AIAA JOURNAL
Vol. 36, No. 12, December 1998

Application of Large-Eddy Simulations and Kirchhoff Method to Jet Noise Prediction

L. Gamet* and J. L. Estivalezes†
ONERA, 31055 Toulouse Cedex, France

The prediction of aerodynamic sound sources and transmission has been the object of new developments. Recent interest in jet acoustics has led to the implementation of highly accurate codes with appropriate inflow and outflow boundary conditions. Nonreflective boundary conditions, based on Thompson's (Thompson, K. W., "Time Dependent Boundary Conditions for Hyperbolic Systems I," *Journal of Computational Physics*, Vol. 68, 1987, pp. 1–24) and Giles' (Giles, M., "Non-Reflecting Boundary Conditions for Euler Equation Calculations," *AIAA Journal*, Vol. 28, No. 12, 1990, pp. 2050–2058) approaches, are coupled with a 2–4 MacCormack interior scheme. The full time-dependent Navier–Stokes equations are solved in the two- or three-dimensional case. Subgrid scale modeling is provided by the second-order velocity structure–function model of Metais and Lesieur (Metais, O., and Lesieur, M., "Spectral Large-Eddy Simulation of Isotropic and Stably Stratified Turbulence," *Journal of Fluid Mechanics*, Vol. 239, 1992, pp. 157–194). Large-eddy simulations of the near field of jet flows can then be used to estimate the sound sources. After the sound sources have been predicted, a linear convective wave equation is used in the outside flow to address the sound transmission. An integral method based on a Kirchhoff surface integral is used to calculate the linear propagation of pressure waves in the far field. It is then possible to obtain the far-field pressure at observation positions at large distances. Results based on axisymmetric and fully three-dimensional near-field calculations of a supersonic jet are presented.

Nomenclature

$\mathcal{A}$	= perturbation amplitude
C	= passive scalar field
c	= sound speed
$\mathcal{D}^*$	= scalar diffusion coefficient
$\mathrm{d}W$	= Riemann variable
E	= total energy
F, G, H	= nonviscous fluxes
F_v, G_v, H_v	= viscous fluxes
L	= length scale
M	= Mach number
$\mathcal{M}$	= maximum Mach number
N	= number of mesh points
$\boldsymbol{n}$	= outward normal vector
P, p	= pressure
Pr	= Prandtl number
$\mathcal{Q}_)$	= subgrid scale heat flux
$\mathcal{R}$	= perfect gases constant
Re	= Reynolds number
r	= radial coordinate
r_{nd}	= random number
S	= control surface
$\mathcal{S}$	= cylindrical source term
Sc	= Schmidt number
T	= temperature
$\mathcal{T}_{ij}$	= subgrid scale tensor
t	= time
$\boldsymbol{U}$	= vector of conservative variables
u, v, w	= velocity components
x	= axial coordinate
β	= Prandtl–Glauert coefficient
γ	= specific heat ratio
Δ_c	= cutoff scale
Δt	= time step
$\Delta x, \Delta r, \Delta\theta$	= grid spacing
η	= reduced coordinate
θ	= azimuthal angle or momentum thickness
μ	= viscosity coefficient
ρ	= density
τ	= retarded time
Ψ	= acoustic variable
Ω	= integration volume

Subscripts

K	= Kirchhoff surface index
0	= Prandtl–Glauert coordinate
1	= reference quantities (centerline)
2	= coflow quantities

Superscript

$*$	= dimensional quantity

Received Feb. 10, 1997; revision received July 13, 1998; accepted for publication July 27, 1998.

*Ph.D. Student, Ecole Nationale de l'Aéronautique et de l'Espace, 10 Avenue Edouard Belin.

†Research Scientist, Centre d'Etudes et de Recherches de Toulouse, Départment pour les Modèles en Aérodynamique et Energétique, 2 Avenue Edouard Belin. Member AIAA.

Introduction

JET noise suppression is one of the challenging tasks for future supersonic flight transport programs. In a first step, accurate prediction of jet noise, and other noise mechanisms, is an essential prerequisite to be able to control or modify flow-generated sounds.

Computational aeroacoustics (CAA) has emerged as a new branch, thanks to recent advances in computational fluid dynamics and to recent progress in computer technology. CAA is concerned with the aerodynamic generation and transmission of sound, starting from the governing equations, which can be taken as the full time-dependent compressible Navier–Stokes equations. From a numerical point of view, difficulties are then centered on an accurate prediction of two main points: sound generation and its transmission to a given observer position in the far field.

The prediction of the sound sources, e.g., sound sources in a jet, can be achieved by means of direct numerical simulations (DNS) (Refs. 1 and 2), where all scales in the flowfield are resolved, or by large eddy simulations (LES) (Refs. 3–6), where only the large-scale components are calculated directly, whereas unresolved scales are modeled. By using these methods, we take all effects into account, including nonlinearity and refraction effects. It is believed that large scales are more efficient than the smaller ones for radiating sound,

which justifies the LES approach for the prediction of sound generation. Some authors have chosen other means to predict the near-field sources: Bailly et al.,[7] Bechara et al.,[8] and Bailly and Lafon[9] used a modified k–ϵ turbulence model coupled with jet noise models to predict the noise radiated from subsonic and supersonic jets.

Once the sound sources have been accurately predicted, several strategies can be used to describe the propagation to the far field. One method would be to directly calculate the sound field by extending the computational domain. Colonius et al.[1] and Mitchell et al.,[2] for example, used DNS to compute the far-field sound generated by shear flows. However, this method requires storage capabilities and CPU resources that are beyond those usually available, particularly in three-dimensional cases. Furthermore, because the acoustic perturbations are quite small, the use of nonlinear equations may result in errors.[10] For this reason, it is better to separate the computation into two domains: the nonlinear near-field, describing the generation of sound, and the linear far field, describing its propagation.

The acoustic analogy is an alternative approach for describing sound propagation. The complete Navier–Stokes equations are rewritten in a wave-type form,[11] reducing the sound problem to an acoustic wave equation associated with a source term involving the Lighthill tensor. The far-field pressure is then given in terms of an integral over the volume containing the sources. The main problem with the acoustic analogy is the difficulty in accounting for refraction effects and shock noise. The use of linearized Euler equations in the far field is a promising method, but this approach has not been tested on many cases. This technique was applied by Viswanathan et al.[12] to supersonic jet noise prediction and also by Mankbadi et al.,[3] Shih et al.,[4] Hixon et al.,[5] and Mankbadi et al.[6] Shih et al.[4] proposed using linearized Euler equations in both the near field and far field. However, in this approach, care must be taken regarding dispersion and diffusion errors of the numerical scheme in the far field. It should also be mentioned for completeness that Shih et al.[13] proposed a zonal method as well.

The Kirchhoff integral method provides an alternative means of solving the noise transmission problem. Here, we also restrict the full computation to the near field and calculate a far-field solution based on a Green's function. The far-field pressure can finally be obtained by an integral over a closed control surface S surrounding the nonlinear sources and involving the pressure and its spatial and temporal derivatives on S. This method is simple and accurate. It has been recently applied to jets aeroacoustics by Lyrintzis and Mankbadi[14] and by Soh.[15] The Kirchhoff method accounts for all phenomena in the flow, namely, nonlinearity, refraction effects, or shock noise. For this reason, it has been chosen for this study. In summary, the physical domain is divided in two parts: the near field, modeled by the full equations, where we perform LES or DNS, and the far field, modeled by a simple wave equation, and recast in an integral formulation (Kirchhoff's formulation). We present the current developments undertaken in this direction and some results of the application of the method to the noise prediction of a hot supersonic jet.

Numerical Algorithm

Governing Equations

The full time-dependent Navier–Stokes equations for three-dimensional fluid motion are written in a nondimensional conservative form. For a three-dimensional cylindrical case, we have

$$\frac{\partial \boldsymbol{U}}{\partial t} + \frac{\partial F}{\partial x} + \frac{\partial rG}{r\partial r} + \frac{\partial H}{r\partial \theta} - \frac{\partial F_v}{\partial x} - \frac{\partial rG_v}{r\partial r} - \frac{\partial H_v}{r\partial \theta} = \mathcal{S} \tag{1}$$

$$\boldsymbol{U} = (\rho, \rho u, \rho v, \rho w, E)^T \tag{2}$$

where F_v, G_v, and H_v are the viscous contributions.

Here u, v, and w are the fluid velocity components in the directions x, r, and θ, respectively, and E is the total energy (sum of the internal and kinetic energy). Nondimensionalization of these equations is with respect to reference quantities, namely, a reference length L^*, velocity U_1^*, density ρ_1^*, temperature T_1^*, and viscosity μ_1^*. L^*/U_1^* is the time reference scale, and $\rho_1^* U_1^{*2}$ is the pressure (and total energy) reference. Using this nondimensional scheme, we introduce the Reynolds number of the flow $Re = \rho_1^* U_1^* L^*/\mu_1^*$ and the Mach number $M = U_1^*/\sqrt{(\gamma \mathcal{R}^* T_1^*)}$, where $\mathcal{R}^* = 287.15$ J kg^{-1} K^{-1}. The Prandtl number, assumed to be constant, is defined by $Pr = \mu^* C_p^*/k^*$, where k^* is the thermal conductivity. The viscosity follows Sutherland's law. The system is completed by the definition of the total energy, written in nondimensional form as

$$E = [p/(\gamma - 1)] + \tfrac{1}{2}\rho(u^2 + v^2 + w^2) \tag{3}$$

and by the perfect gas law

$$p/\rho = T/\gamma M^2 \tag{4}$$

In all simulations, to enhance visualization, a passive scalar field C was also computed. The nondimensional form of the equation for this scalar field is

$$\frac{\partial(\rho C)}{\partial t} + \frac{\partial(\rho C u)}{\partial x} + \frac{1}{r}\frac{\partial(r\rho C v)}{\partial r} + \frac{1}{r}\frac{\partial(\rho C w)}{\partial \theta} = \frac{1}{ReSc} \times \left\{ \frac{\partial}{\partial x}\left(\mu \frac{\partial C}{\partial x}\right) + \frac{1}{r}\frac{\partial}{\partial r}\left(\mu \frac{1}{r}\frac{\partial C}{\partial r}\right) + \frac{1}{r}\frac{\partial}{\partial \theta}\left(\mu \frac{1}{r}\frac{\partial C}{\partial \theta}\right) \right\} \tag{5}$$

with the Schmidt number Sc defined by $Sc = \mu^*/\rho^* D^*$, where D^* is the diffusion coefficient for the scalar field C.

Numerical Scheme

Equations are solved using a finite volume, high-order extension of MacCormack's scheme due to Gottlieb and Turkel.[16] This scheme has already been used by many authors for boundary-layer simulations,[17,18] for mixing layer simulations,[19–21] and for supersonic jet flow studies.[6] Moreover, this scheme has been successfully used for aeroacoustics computations.[22] Based on predictor corrector phases, the scheme is explicit, second-order accurate in time and fourth-order in space. The time step Δt follows a Courant–Friedrichs–Lewy condition and Fourier criteria. Extension to three dimensions and to the complete fluid motion equations is done through a directional splitting sequence:

$$\begin{aligned} U^{n+2} &= L_{\theta v}^- L_{rv}^- L_{xv}^- L_\theta^- L_r^- L_x^- L_{\theta v}^+ L_{rv}^+ L_{xv}^+ L_\theta^+ L_r^+ L_x^+ U^n \\ U^{n+4} &= L_{xv}^+ L_{rv}^+ L_{\theta v}^+ L_x^+ L_y^+ L_\theta^+ L_{xv}^- L_{rv}^- L_{\theta v}^- L_x^- L_y^- L_\theta^- U^{n+2} \end{aligned} \tag{6}$$

where L_x, L_y, L_θ, L_{xv}, L_{rv}, and $L_{\theta v}$ correspond to the implementation of F, G, H, F_v, G_v, and H_v, respectively. L_i^+ (with $i = x$, r, or θ) refers to a sweep in the direction i with forward predictor and backward corrector. The alternate version L_i^- employs a backward predictor and forward corrector.

Because a cylindrical coordinate system has been used, the area of the interface becomes zero for cells on the axis. This means that interfacial fluxes also become zero on the axis in the L_r and L_{rv} sweeps. On all other boundaries, a nonreflective treatment is applied at the end of each nonviscous sweep. This is discussed in the next section.

Boundary Conditions

The values of flux vectors at nodes situated two cells outside the computational domain are needed at cells close to the left- and right-side boundaries. Third-order extrapolations are used to obtain fluxes at these phantom cell centers outside the computational domain, for instance, at grid points $N+1$, $N+2$, -2, and -1 in the case of a one-dimensional grid with N points. It should be noted that extrapolating fluxes is equivalent to using one-sided differences. The procedure was to use the following third-order extrapolation, for instance, for a forward sweep:

$$\begin{aligned} F_{N+1} &= 4F_N - 6F_{N-1} + 4F_{N-2} - F_{N-3} \\ F_{N+2} &= 4F_{N+1} - 6F_N + 4F_{N-1} - F_{N-2} \end{aligned} \tag{7}$$

Similar extrapolations were used to obtain fluxes at points -1 and -2 for a backward sweep. With these extrapolations, the scheme can be advanced in time at the boundaries, from time step n to $n+1$. Time changes of the characteristic variables W_i for each eigenvalue are then determined at the boundaries. The equations were linearized

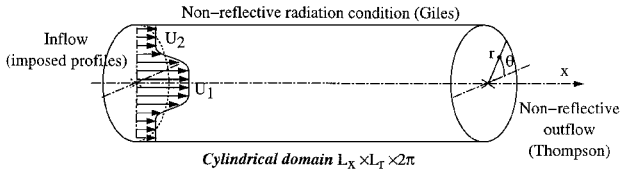

Fig. 1 Cylindrical computational domain used in jet flow computations.

at each time step, and the characteristic variables normal to the boundary were considered. Boundary treatment was based on the inviscid equations. In particular, at a $x = Cte$ boundary, we have

$$\begin{aligned} \mathrm{d}W_1 &= \mathrm{d}p - \tilde{c}^2\,\mathrm{d}\rho, \qquad & \mathrm{d}W_2 &= \mathrm{d}\boldsymbol{u}\cdot\boldsymbol{n}_1 \\ \mathrm{d}W_3 &= \mathrm{d}\boldsymbol{u}\cdot\boldsymbol{n}_2, \qquad & \mathrm{d}W_4 &= \mathrm{d}p + \tilde{\rho}\tilde{c}\,\mathrm{d}\boldsymbol{u}\cdot\boldsymbol{n} \\ \mathrm{d}W_5 &= \mathrm{d}p - \tilde{\rho}\tilde{c}\,\mathrm{d}\boldsymbol{u}\cdot\boldsymbol{n}, \qquad & \mathrm{d}W_6 &= \mathrm{d}C \end{aligned} \tag{8}$$

for each eigenvalue λ_i with $\lambda_1 = \lambda_2 = \lambda_3 = \lambda_6 = \boldsymbol{u}\cdot\boldsymbol{n}$, $\lambda_4 = \boldsymbol{u}\cdot\boldsymbol{n} + c$, and $\lambda_5 = \boldsymbol{u}\cdot\boldsymbol{n} - c$, where $\boldsymbol{n}$ is the boundary outward normal. Outward normal vectors $(\boldsymbol{n}, \boldsymbol{n}_1, \boldsymbol{n}_2)$ form an orthonormal base, with $(\boldsymbol{n}_1, \boldsymbol{n}_2)$ in the plane tangent to the boundary. Characteristic variables W_1–W_6 refer to the entropy wave, the tangential velocity component waves, + and − acoustic waves, and the passive scalar field wave, respectively. The symbol $\sim$ refers to an approximation of a given variable, taken as its value at time step n.

In jet flow simulations (Fig. 1), we considered three types of boundary conditions: inflow, outflow, and radiation. The distinction between a radiation condition and an inflow/outflow is made in the sense that radiation refers to a boundary with zero mean velocity perpendicular to the boundary.

The characteristic boundary procedures are applied after each nonviscous sweep, for the corresponding boundary ($x = Cte$ after L_x sweep, etc.). We impose the time variation of the characteristic variables $\mathrm{d}W_i$ (presented in the following paragraphs), and then invert the equation system (8), where the unknowns are now $\mathrm{d}q = q^{n+1} - q^n$ (with $q = \rho,\ p,\ \boldsymbol{u}\cdot\boldsymbol{n}, \boldsymbol{u}\cdot\boldsymbol{n}_1, \boldsymbol{u}\cdot\boldsymbol{n}_2, C$), thus, obtaining corrected variables q at time step $n+1$ on the boundary. The suitability of such boundary conditions for jet flow computations and aeroacoustic purposes has been extensively tested and much work can be found in the literature, for example, see Refs. 23–27.

Inflow and Outflow Boundary Conditions

Following Thompson,[28,29] a characteristic-based boundary condition procedure is used to obtain the correct boundary values at inflow and outflow. The treatment consists of setting to zero the time variation of any characteristic variable corresponding to an incoming wave ($\lambda_i < 0$).

At a supersonic inflow, all data are given, so that all time variations of the characteristic variables are set to zero because all waves are incoming waves. At a supersonic outflow, all data can be extrapolated from the interior domain, so that all time variations of the characteristic variables are calculated using Eqs. (8). At a nonreflective subsonic inflow, the outgoing acoustic wave $\mathrm{d}W_4$ is calculated as in Eq. (8), and all other $\mathrm{d}W_i$ are set to zero. The described formulation also allows certain inflow profiles to be imposed. For instance, at a subsonic inflow, imposing u velocity and density profiles will consist in imposing combinations of the outgoing characteristic time variations to the incoming characteristic time variations as follows:

$$\mathrm{d}W_1 = \mathrm{d}W_4, \qquad \mathrm{d}W_5 = \mathrm{d}W_4$$

with $\mathrm{d}W_4$ calculated as in Eq. (8). At an outflow, setting time derivatives of the characteristic variables to zero for those eigenvalues corresponding to incoming waves will give the boundary a nonreflective character. In other words, we set $\mathrm{d}W_5$ to zero at a subsonic outflow.

Note that this approach is only purely nonreflecting for waves that have a direction of propagation normal to the boundary.

Radiation Boundary Conditions

At an $r = r_{\max}$ boundary, the cylindrical source terms $\mathcal{S}$ have to be introduced in Eqs. (8). This modifies the time variations of the + and − acoustic waves in the following way:

$$\begin{aligned} \mathrm{d}W_4 &= \mathrm{d}p + \tilde{\rho}\tilde{c}\,\mathrm{d}v + (\tilde{\rho}\tilde{c}/r)(\tilde{c}\tilde{v} - \tilde{w}^2)\Delta t \\ \mathrm{d}W_5 &= \mathrm{d}p - \tilde{\rho}\tilde{c}\,\mathrm{d}v + (\tilde{\rho}\tilde{c}/r)(\tilde{c}\tilde{v} + \tilde{w}^2)\Delta t \end{aligned} \tag{9}$$

Giles'[30–32] boundary treatment was used as a radiation boundary condition for jet flow computations. This method is based on a Fourier analysis of the linearized Euler equations at the boundary. In summary, it consists of the introduction of tangential effects for the nonreflecting treatment of the incoming acoustic wave, instead of setting its time variation to zero:

$$\begin{aligned} \mathrm{d}W_5 = \Delta t\Bigg[&-\tilde{v}\tilde{\rho}\tilde{c}\frac{\partial u}{\partial x} - \tilde{v}\tilde{\rho}\tilde{c}\frac{\partial w}{r\,\partial\theta} - \tilde{u}\left(\frac{\partial p}{\partial x} - \tilde{\rho}\tilde{c}\frac{\partial v}{\partial x}\right) \\ &- \tilde{w}\left(\frac{\partial p}{r\,\partial\theta} - \tilde{\rho}\tilde{c}\frac{\partial v}{r\,\partial\theta}\right)\Bigg] \end{aligned} \tag{10}$$

Mean Pressure Condition

At outflow and radiation boundaries, we have added a correction to the incoming acoustic wave for a subsonic outflow to prevent the average pressure of the solution in the domain from drifting. Following Poinsot and Lele,[33] this pressure correction is implemented by

$$\mathrm{d}W_5 = \mathrm{d}W_{5_{\text{exact}}} - \Delta t\,\underbrace{\sigma(1-\mathcal{M}^2)c/L}_{K}(p - p_\infty) \tag{11}$$

where the first term on the right-hand side, $\mathrm{d}W_{5_{\text{exact}}}$, is calculated by Giles'[30–32] or Thompson's[28,29] approach, developed in the preceding paragraphs. The form of the constant K was originally proposed by Rudi and Strikwerda.[34] $\mathcal{M}$ is the maximum Mach number in the flowfield, L is a characteristic size of the domain, p_∞ is the mean pressure at infinity, and σ is a constant with value 0.15, following Ref. 33.

Subgrid Scale Modeling

Filtering of the Equations

DNS is based on a discretization of the complete Eq. (1). The governing equations for LES are obtained by applying a spatial filter to the system (1). A filter operation extracts the large-scale components $\bar{q}$ of a given continuous variable q through the convolution of q with a grid filter function Φ_Δ:

$$\bar{q}(\boldsymbol{x}) = \int_{(\Omega)} \Phi_\Delta(\boldsymbol{x} - \boldsymbol{\xi}) q(\boldsymbol{\xi})\,\mathrm{d}\boldsymbol{\xi} \tag{12}$$

where Ω is the flow domain and Δ is the filter width of the kernel Φ_Δ, which is normalized such that the integral of Φ_Δ over Ω equals 1. For compressible flows, the equivalent of Favre filtering is introduced by $\tilde{q} = \overline{\rho q}/\bar{\rho}$.

The convolution bar-filter is then applied to the Navier–Stokes equations (1). We will assume that the bar-filter commutes with the partial differential operators ∂/∂_t and ∂/∂_{x_i}. In a general context, the filter operation does not strictly commute with the partial differential operators, giving rise to additional terms in the LES equations.[35] A number of unknown terms such as $\overline{\rho u_i u_j}$ or $\overline{(E+p)u_i}$ appear in the filtered equations and require modeling. We will simply recall here the main milestones of the closure procedure applied in this study. More details can be found in Refs. 18 and 36–38.

Closure of the System

First, modeling of all of the viscous unknown contributions, arising from the filtering of F_v, G_v, and H_v, is simply obtained by replacing these unknown terms by their corresponding terms evaluated in the filtered fields. For the F, G, and H contributions, we have chosen a pragmatic approach, which consists in modeling the terms $\overline{\rho u_i u_j}$ and $\overline{(E+p)u_i}$ by the sum of their directly accessible counterparts and an evaluation of the influence of the subgrid scales

on the resolved motion via a turbulent viscosity μ_t and a turbulent thermal conductivity k_t, respectively (obtained from μ_t with a turbulent Prandtl number). We have

$$\overline{\rho u_i u_j} = \bar{\rho}\tilde{u}_i\tilde{u}_j + \underbrace{[\overline{\rho u_i u_j} - \bar{\rho}\tilde{u}_i\tilde{u}_j]}_{\mathcal{T}_{ij}}$$
$$\overline{(E+p)u_i} = (\bar{E}+\bar{p})\tilde{u}_i + \underbrace{[\overline{(E+p)u_i} - (\bar{E}+\bar{p})\tilde{u}_i]}_{\mathcal{Q}_i} \tag{13}$$

where $\mathcal{T}_{ij}$ is the usual subgrid-stress tensor and $\mathcal{Q}_i$ is the subgrid heat-flux vector. Following Erlebacher et al.[39] and Ducros et al.,[38] we make the assumption that the isotropic part of the subgrid-stress tensor can be neglected. With the aid of eddy viscosity and diffusivity models, closure of the system is obtained in the form

$$\mathcal{T}_{ij} = \mathcal{T}_{ij} - \tfrac{1}{3}\mathcal{T}_{ll}\delta_{ij} + \underbrace{\tfrac{1}{3}\mathcal{T}_{ll}\delta_{ij}}_{\approx 0} \approx (\mu_t/\tilde{\mu})\widetilde{\mathcal{T}_{ij}}$$
$$\mathcal{Q}_i \approx -\frac{\mu_t}{(\gamma-1)M^2 Pr_t}\frac{\partial \tilde{T}}{\partial x_i} \tag{14}$$

The tensor $\widetilde{\mathcal{T}_{ij}}$ is the strain rate tensor, taken for filtered variables.

Subgrid Scale Model

The last step of the modeling is to determine the turbulent eddy viscosity μ_t. The subgrid scale model that we have implemented is based on the second-order velocity structure function model developed by Metais and Lesieur[40] and Lesieur et al.[41] The behavior of this model, when tested on decreasing homogeneous turbulence, is similar to the classical Smagorinsky model. This model introduces an eddy viscosity calculated from a spectral eddy viscosity[42,43] obtained from a kinetic energy spectrum local in space[40]:

$$\nu_t(\boldsymbol{x}, t) = \frac{\mu_t(\boldsymbol{x}, t)}{\bar{\rho}} = C_m \Delta_c \sqrt{\widetilde{F_2}(\boldsymbol{x}, \Delta_c, t)} \tag{15}$$

where $\widetilde{F_2}(\boldsymbol{x}, \Delta_c, t)$ is the second-order velocity structure function given by

$$\widetilde{F_2}(\boldsymbol{x}, \Delta_c, t) = \langle \|\tilde{\boldsymbol{u}}(\boldsymbol{x}+\boldsymbol{r}, t) - \tilde{\boldsymbol{u}}(\boldsymbol{x}, t)\|^2 \rangle_{\|\boldsymbol{r}\| = \Delta_c} \tag{16}$$

The model assumes that the subgrid scales turbulence follows a Kolmogorof cascade. Following Chollet and Lesieur,[43] we take $Pr_t = 0.6$ and $C_m = 0.063$. In Eq. (16), $\langle\,\rangle$ refers to a space average computed over the six neighboring points, and Δ_c is a local measure of the mesh size:

$$\Delta_c = \max(\Delta_x, \Delta_r, r\Delta_\theta) \tag{17}$$

In its original form, this model was found to be too sensitive to the large scales of motion in the flowfield, providing too much eddy viscosity during the early stages of transition in a shear flow. We have, therefore, implemented the filtered structure function model,[18,37] where a high-pass filter (a discrete Laplacian filter iterated three times) is applied to the resolved velocity field before computing its structure function. The constant C_m is then set to 8.4×10^{-4}.

This model offers much better behavior in compressible boundary-layer transition[38,40,44,45] and in shear flow configurations[46] than the Smagorinsky model.

Kirchhoff Method

Having calculated the nonlinear sources from the numerical method described, the far-field pressure variations (or any other acoustic variable) are obtained by integrating over a control surface S, as shown in Fig. 2. Outside the control surface, the flow is moving at a uniform subsonic speed U_∞ and is governed by the convective wave equation:

$$\nabla^2\Psi - \frac{1}{c_\infty^2}\left(\frac{\partial}{\partial t} + U_\infty\frac{\partial}{\partial x}\right)^2\Psi = 0 \tag{18}$$

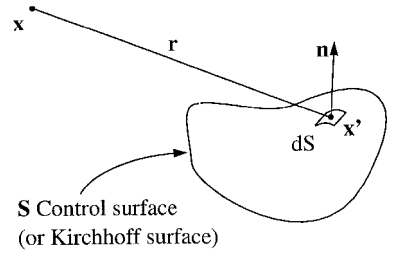

Fig. 2 Kirchhoff surface in the general case.

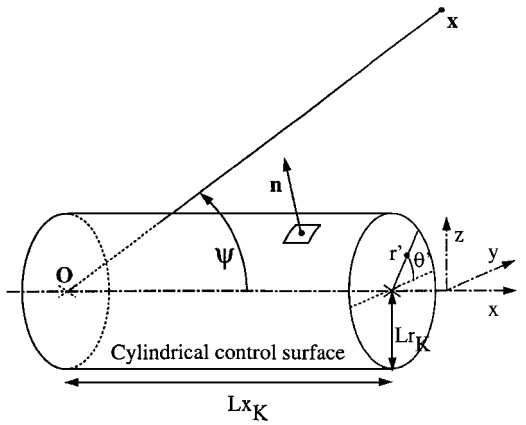

Fig. 3 Cylindrical Kirchhoff surface used in jet flow computations.

where Ψ is any quantity satisfying the wave equation, e.g., acoustic pressure. This equation is solved in terms of a Green's function. The solution at an observer point $\boldsymbol{x} = (x, y, z)$ outside S can be obtained in the final form[47]

$$\Psi(\boldsymbol{x}, t) = \frac{1}{4\pi}\iint_{S_0}\left[\frac{\Psi}{r_0^2}\frac{\partial r_0}{\partial n_0} - \frac{1}{r_0}\frac{\partial \Psi}{\partial n_0}\right.$$
$$\left. + \frac{1}{c_\infty r_0 \beta^2}\frac{\partial \Psi}{\partial \mathcal{T}}\left(\frac{\partial r_0}{\partial n_0} - M_\infty\frac{\partial x_0}{\partial n_0}\right)\right]_{\mathcal{T}} \mathrm{d}S_0 \tag{19}$$

where subscript 0 is the Prandtl–Glauert coordinate transformation defined by

$$x_0 = x, \qquad y_0 = \beta y, \qquad z_0 = \beta z \tag{20}$$

with $\beta = \sqrt{(1 - M_\infty^2)}$, and r_0 is the distance between the observer position and a point on the surface in the Prandtl–Glauert system

$$r_0 = \sqrt{(x-x')^2 + \beta^2[(y-y')^2 + (z-z')^2]} \tag{21}$$

Here, $\boldsymbol{x}' = (x', y', z')$ refers to a point on the control surface. Vector $\boldsymbol{n}_0$ is the outward pointing normal to the surface in the Prandtl–Glauert system. The term $\partial r_0/\partial n_0$ can be evaluated by $\partial r_0/\partial n_0 = \boldsymbol{n}\cdot\nabla_0 r_0$, with $\boldsymbol{n}$ the outward pointing vector normal to the surface in physical space.

The terms in $[\,]_{\mathcal{T}}$ are to be evaluated at the retarded time $t - \mathcal{T}$ with

$$\mathcal{T} = \frac{r_0 - M_\infty(x - x')}{c_\infty \beta^2} \tag{22}$$

The method requires only first-order derivatives on the control surface and so is easily implemented. It has recently been reviewed by Lyrintzis[48] and applied to jet aeroacoustics by Lyrintzis and Mankbadi[14] and Soh.[15] More details of the method can be found in those references.

In the case of jets, the Kirchhoff surface is taken to be a cylinder of radius L_{rK} and length L_{xK} (Fig. 3), included in the cylindrical calculation domain. Kirchhoff's hypotheses are no longer valid for the ends of this cylinder because they lie in a nonlinear domain.

In our calculations, the contribution to the surface integral from the cylinder ends has, therefore, been neglected. We estimate[25] that using an open Kirchhoff surface implies a 5–8% error in the far-field sound prediction, the maximum error occurring at observer positions close to the jet axis. Freund et al.[49] have recently examined means of improving the accuracy of the Kirchhoff integral solution in the case of open surfaces, but these improvements have not been implemented in the current work.

Jet Noise Calculations

Simulation Parameters

The simulations presented show results of jet noise calculations on a hot jet at Mach number $M = 2$, temperature $T_1^* = 760\,\mathrm{K}$, and velocity $U_1^* = 1115\,\mathrm{ms}^{-1}$ at nozzle exit. The jet exits in a quiescent medium at temperature $T_2^* = 280\,\mathrm{K}$, and the nozzle radius R^* is 4.572 cm. Subscript 1 refers to centerline quantities and subscript 2 to quantities at $r \to \infty$. The flow is assumed to be pressure balanced. This case is taken from the experiments of Seiner and Ponton[50] and Seiner[51] to compare the results from the calculation to available experimental data.

Here the reference quantities used in the nondimensionalization of the Navier–Stokes equations are the nozzle radius R^*, the velocity U_1^*, density ρ_1^*, temperature T_1^*, and viscosity μ_1^* at the nozzle exit on the jet centerline. The Reynolds number of the flow is then defined by $Re = \rho_1^* U_1^* R^*/\mu_1^*$. The Schmidt number is taken to be unity, and the Prandtl number $Pr = 0.7$.

The spatial simulations are obtained with the numerical method described in the Numerical Scheme section, using axisymmetric and fully three-dimensional formulations. At the inflow, we impose a half-Gaussian mean velocity profile[50] $\langle u \rangle$ of a given momentum thickness

$$\begin{aligned} \langle u \rangle_{(r)} &= U_2, \qquad r \le h \\ \langle u \rangle_{(r)} &= U_2 + (U_1 - U_2)\exp[-(\ell_n 2)\eta^2], \qquad r > h \end{aligned} \tag{23}$$

with

$$\eta = (r - h)/(1 - h) \tag{24}$$

where h is the radius of the potential core at inflow and is calculated by an iterative method so that the compressible momentum thickness θ_0 at inflow is imposed and θ_0 is defined by

$$\theta_0 = \int_0^{+\infty} \langle \rho \rangle_{(r)} \frac{\langle u \rangle_{(r)} - U_2}{U_1 - U_2}\left[1 - \frac{\langle u \rangle_{(r)} - U_2}{U_1 - U_2}\right] \mathrm{d}r \tag{25}$$

U_2 was taken to be 0.01 to avoid numerically indeterminate boundary conditions. The density profile $\langle \rho \rangle$ at inflow is imposed and is calculated from the velocity profile by the mean of a Crocco–Busemann relation.

Nonreflective boundary conditions, as earlier presented, are applied on all other boundaries. Thompson-like conditions[28,29] are applied at the outflow, and Giles' conditions[30–32] are applied at $r = r_{\max}$.

Random velocity perturbations of low amplitude are superimposed on the inflow profiles

$$\begin{aligned} u'(r) &= \mathcal{A} r_{nd}\sqrt{0.95\,e^{-\xi^2} + 0.05(1 - \tanh\xi)} \\ v'(r) &= \mathcal{A} r_{nd}\sqrt{e^{-\xi^2}}, \qquad w'(r) = \mathcal{A} r_{nd}\sqrt{e^{-\xi^2}} \end{aligned} \tag{26}$$

with

$$\xi = (1/4\theta_i)[r - (1/r)]$$

where $\mathcal{A}$ is of the order of 0.01. Perturbations on the tangential velocity component are set to zero in the axisymmetric simulations.

Once the initial conditions are evacuated, the far-field pressure is calculated using Kirchhoff's method at a number of observation points situated in a plane including the jet axis and on a circle of radius 80 (R^*) centered on the origin of the domain at the nozzle exit on the axis. Kirchhoff's surface is a cylinder of radial and axial dimensions L_{rK} and L_{xK} equal to the domain size (except in the subsequent three-dimensional case). As has been shown by Lyrintsis,[48] the radial position of the Kirchhoff surface is $L_{rK} = 6$.

Axisymmetric Calculations

Preliminary results were obtained with axisymmetric DNS calculations at $Re = 1000$, on a 40×6 (radii) domain, with 344×120 grid points. The grid is stretched in the radial direction with a concentration of grid points near the shear layer zone ($r = 1$). Inside the shear layer 40 grid points have been placed because of the sharp flow gradients in this zone at the nozzle exit. This grid resolution is sufficient to perform two-dimensional DNS of this flow for the Reynolds number investigated. The present computation uses 40 points per wavelength, based on a estimated maximum Strouhal number of 0.4.

This two-dimensional DNS calculation at quite low Reynolds number is motivated by the fact that two-dimensional axisymmetric LES calculations have no real meaning and are not relevant. Indeed, subgrid scale modeling is based on the three dimensionality of the subgrid scale turbulence, and so a two-dimensional axisymmetric LES simulation cannot reproduce the development of helicoidal instability existing in such flows. The LES approach must be used with fully three-dimensional simulations.

The inflow momentum thickness was set to $\frac{1}{19}$, which represents a larger value than the experimental value, supposed equal to zero.[51]

Figures 4 and 5 show the overall sound pressure level (OASPL) far-field acoustic data and Strouhal dependence on inclination to jet

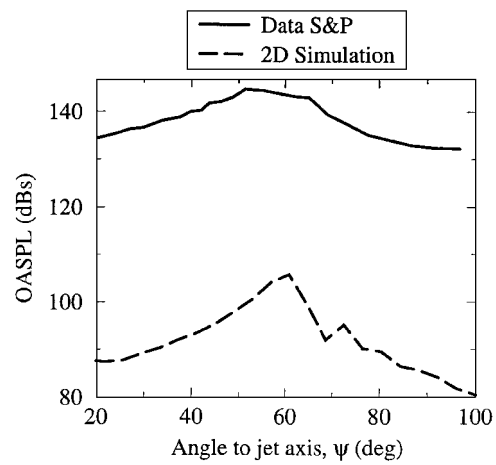

Fig. 4 OASPL vs angle to jet axis in the two-dimensional axisymmetric simulation; $\psi = 0$ corresponds to the jet axis itself.

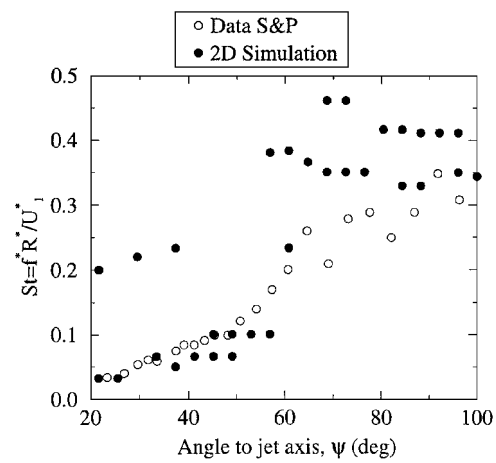

Fig. 5 Dominant Strouhal number vs angle to jet axis in the two-dimensional axisymmetric simulation; $\psi = 0$ corresponds to the jet axis itself.

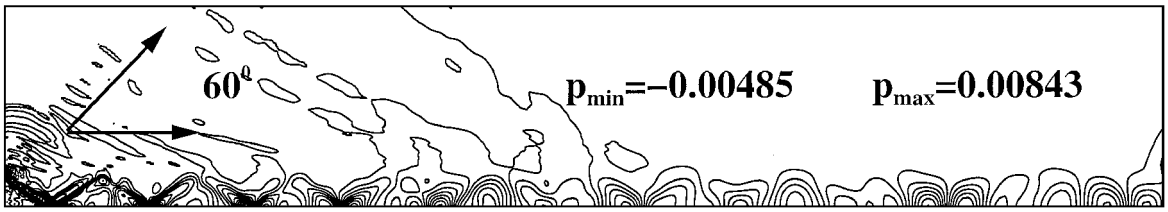

Fig. 6 Instantaneous isocontours of the pressure fluctuation field in the 2D axisymmetric simulation ($p - p_{\text{mean}}$).

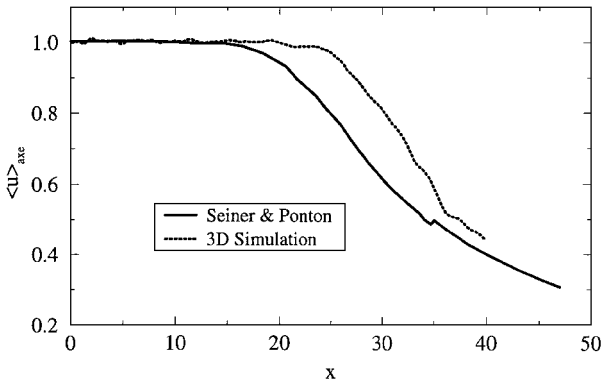

Fig. 7 Mean velocity along the jet centerline in three-dimensional cylindrical simulation.

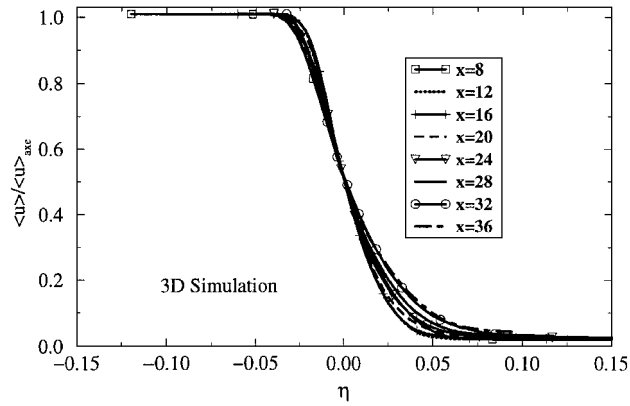

Fig. 8 Averaged velocity profiles as a function of reduced radial coordinate η in three-dimensional cylindrical simulation.

axis (see ψ in Fig. 3). Experimental data are also plotted on the same graph. Numerical data seem to be shifted by 35 dB, which could be explained by the axisymmetric approximation and the low Reynolds number used in this DNS. The frequency data exhibit a few points at low angles that are most likely in error, and a large amount of scatter can be seen at large angles. However, the general trend in amplitude and frequency variation seems to be recovered by the axisymmetric simulation.

An instantaneous photograph of the fluctuating pressure field ($p - p_{\text{mean}}$) is shown in Fig. 6, showing that the near flowfield is dominated by directional Mach wave emissions at an angle near 60 deg. This is in agreement with the experiments of Seiner and Ponton.[50] It is well known that supersonic jets produce intense noise when their structures are convected supersonically relative to the ambient sound speed. This phenomenon was first described by Phillips[52] and Ffowcs Williams.[53] The experimental results of Oertel,[54,55] later predicted by the instability study of Tam and Hu,[56] clearly show the existence of three families of Mach waves. The waves observed here appear to correspond to the Kelvin–Helmholtz family of instability described in Ref. 56.

Three-Dimensional Cylindrical Calculations

Even if general trends are recovered, the axisymmetric simulations do not compare very favorably with the experiments, for example, the impossibility with axisymmetric simulations to develop three-dimensional helical instability as can be seen in experiments.

Therefore, further efforts were made by computing fully three-dimensional cylindrical LES at $Re = 3 \times 10^4$ for the same case. The size of the domain is $40 \times 6 \times 2\pi$, with $144 \times 50 \times 40$ mesh points in the axial, radial, and azimuthal directions. The grid is stretched in the radial direction. Inside the shear layer 20 grid points are placed because of the sharp flow gradients in this zone at the nozzle exit. Indeed, LES calculation of three-dimensional temporal round jets have shown[25] that, for the Reynolds number considered, this grid resolution is sufficient to capture the large-scale structures of this kind of flow. However, due to the high computational cost of this type of simulation, it seems to be difficult to perform systematic grid-independent study.

The present computation uses 40 points per wavelength, based on a estimated maximum Strouhal number of 0.4. Inflow momentum thickness is taken to be $\frac{1}{10}$, due to the coarser resolution of the mesh, compared to the axisymmetric case. Figures 7 and 8 show mean velocity variation along the jet axis and averaged velocity profiles plotted vs the reduced radial coordinate $\eta = (r - r_{1/2})/x$, where $r_{1/2}$ is the radius to half-velocity. The potential core predicted by the simulation is shorter by 9 radii than the experimental one. This is to be expected because the actual experimental momentum thickness at inflow is close to zero.

Figure 9 shows other, often presented statistics, calculated in cylindrical coordinates. All of the profiles look similar except the $\langle u'w' \rangle$ and $\langle v'w' \rangle$ cross-correlations profiles. These suggest that u' and w' are not correlated, and likewise for v' and w'. Unfortunately, comparisons with the experiment were not possible for these statistics because they were not published and, perhaps, not measured.

Far-field data were obtained using two different cylindrical Kirchhoff surfaces: one with $L_{rK} \lesssim 6$, $L_{xK} = 30$, and the other with $L_{rK} \lesssim 6$, $L_{xK} = 40$. OASPL and Strouhal dependence on the angle to the jet axis are shown in Figs. 10 and 11 for the three-dimensional cylindrical calculation. The directivity of the generated sound is improved compared with the axisymmetric calculations, although it is shifted toward the low angles in the computation. The general trend in the peak Strouhal angular dependence is also recovered. Some scatter in the data can be observed, particularly at large angles, as in the experiment. However, longer recorded signals would provide a finer spectral analysis at large angles. Note that the present calculation was expensive, and took about 10 weeks on a R-4000 SGI workstation. A better agreement in amplitude with the experiment can be obtained with a Kirchhoff surface shorter than the total domain axial size. This observation has not been fully explained and is currently the object of further work. Possible explanations could be found in the Thompson's boundary conditions[28,29] used at outflow, which are not perfectly nonreflecting for nonplanar waves, or in a bad transition to turbulence near the outflow, which could be due to the relatively coarse grid used in the simulation.

The flowfield close to the nozzle exit is dominated by Mach wave emissions (not show here), but Figs. 12 and 13 show the obvious three dimensionality of the flow features downstream. The axial vorticity isosurface in Fig. 13 also shows that vortical structures are strongly stretched in the axial direction.

As a general conclusion, a better agreement with the experiments is obtained using fully three-dimensional simulations, compared to the results of the preceding section.

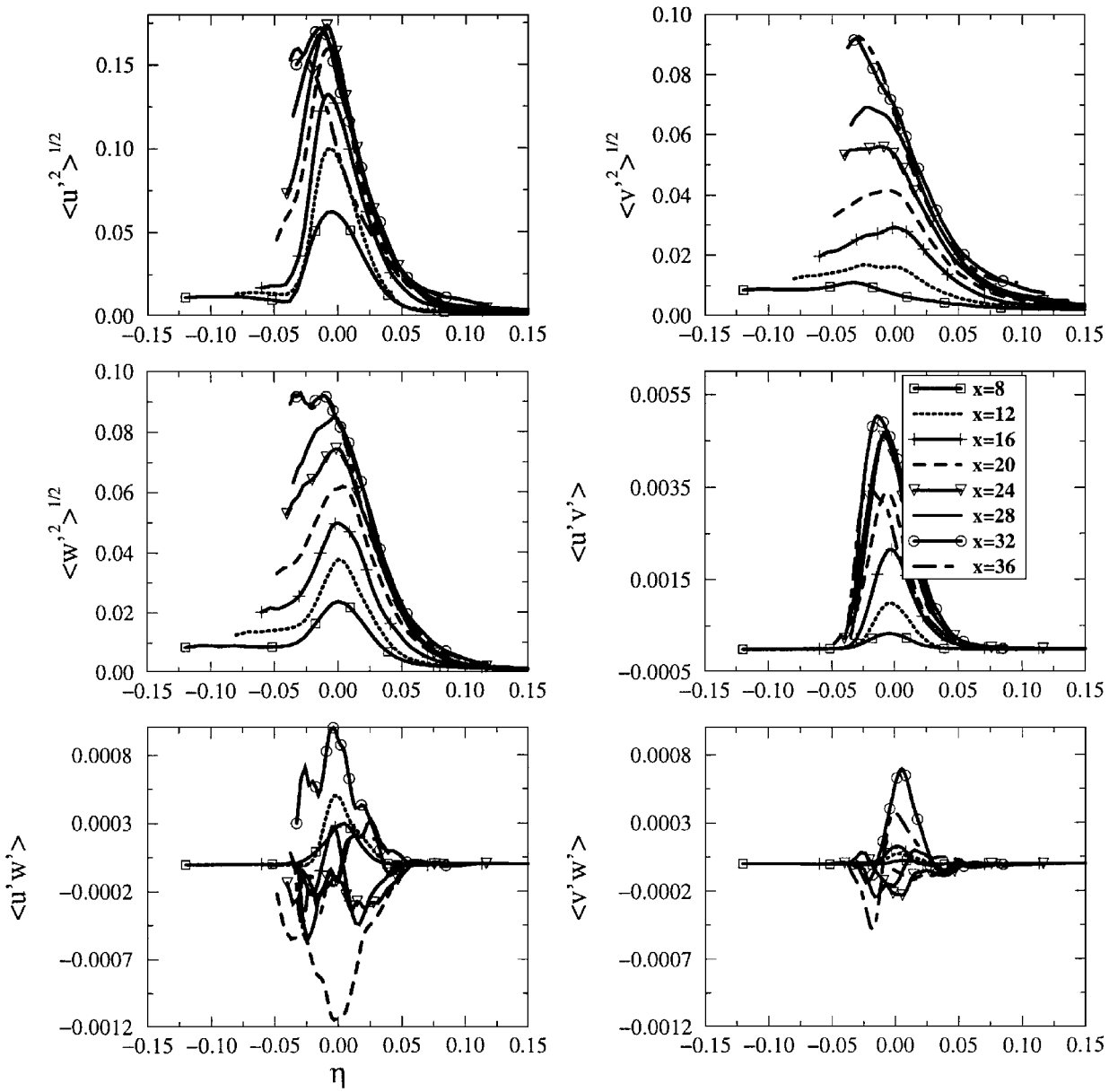

Fig. 9 Statistics in the three-dimensional cylindrical simulation, as a function of the reduced variable η.

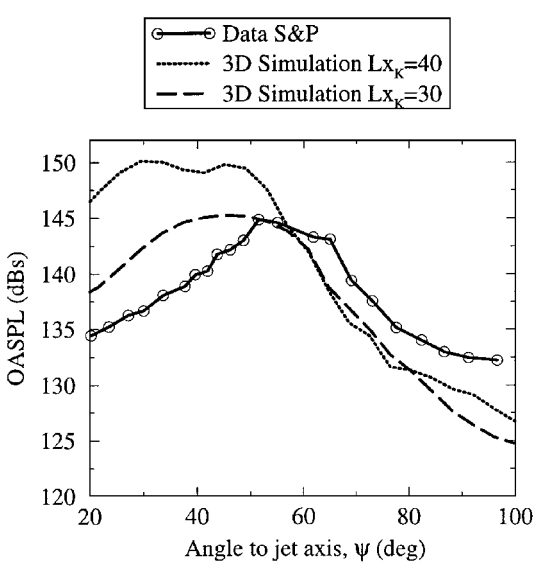

Fig. 10 OASPL vs angle to jet axis in the three-dimensional cylindrical simulation; two different lengths are used for the Kirchhoff's control surface: $L_{xK} = 30$ and $L_{xK} = 40$; $\psi = 0$ corresponds to the jet axis itself.

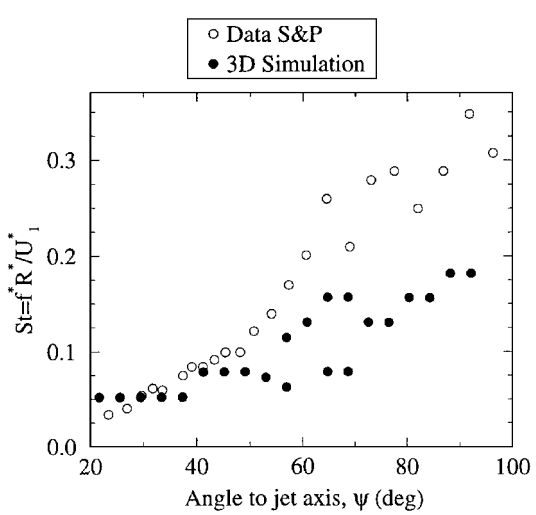

Fig. 11 Dominant Strouhal number vs angle to jet axis in the three-dimensional cylindrical simulation; two different lengths are used for the Kirchhoff's control surface: $L_{xK} = 30$ and $L_{xK} = 40$; $\psi = 0$ corresponds to the jet axis itself.

Fig. 12 Instantaneous isosurfaces of passive scalar field (isosurface $C = 0.5$) in the three-dimensional cylindrical simulation.

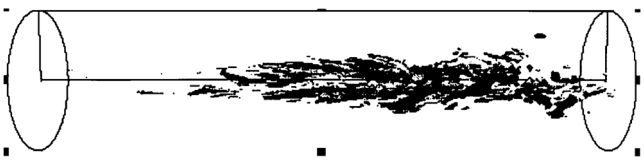

Fig. 13 Instantaneous isosurfaces axial vorticity (dark gray $\omega_x = 0.6$, light gray $\omega_x = -0.6$) in the three-dimensional cylindrical simulation.

Conclusion

A jet noise prediction method using LES or DNS in the near field and an acoustic approximation based on a Kirchhoff method in the far field has been presented. Near-field computations, shown here for an example of a supersonic jet flow at $M = 2$, are performed using a highly accurate 2–4 MacCormack numerical scheme, a subgrid-scale model based on the second-order velocity structure function to perform LES, and non-reflective boundary conditions based on the approach of Thompson and Giles. The propagation of the acoustic pressure in the far field is modeled by a Kirchhoff integral. The method is simple and accurate and can be summarized by the calculation of a surface integral on a control surface S surrounding all of the nonlinear sources and requiring the pressure and its derivatives on S.

Finally, an application of the method is shown, and results are presented of jet noise prediction on a supersonic jet flow at $M = 2$, using both axisymmetric and fully three-dimensional calculations. Results are compared to experimental data. LES of the fully three-dimensional equations show more promising results than axisymmetric simulations, which cannot take into account the inevitable three dimensionality of highly compressible flows.

References

[1]Colonius, T., Lele, S. K., and Moin, P., "Direct Computation of the Sound Generated by a Two-Dimensional Shear Layer," AIAA Paper 93-4328, Oct. 1993.

[2]Mitchell, B. E., Lele, S. K., and Moin, P., "Direct Computations of the Sound Generated by Vortex Pairing in an Axisymmetric Jet," AIAA Paper 95-0504, Jan. 1995.

[3]Mankbadi, R. R., Shih, S. H., Hixon, D. R., and Povinelli, L. A., "On the Use of Linearized Euler Equations in the Prediction of Jet Noise," AIAA Paper 95-0505, Jan. 1995.

[4]Shih, S. H., Hixon, D. R., Mankbadi, R. R., and Povinelli, L. A., "Prediction of Flow and Acoustic Fields of a Supersonic Jet," AIAA Paper 96-0751, Jan. 1996.

[5]Hixon, D. R., Shih, S. H., and Mankbadi, R. R., "Effect of Input Disturbance on Linearized Euler Equation Prediction of Jet Noise," AIAA Paper 96-0752, Jan. 1996.

[6]Mankbadi, R. R., Hayder, M. E., and Povinelli, L. A., "The Structure of Supersonic Jet Flow and Its Radiated Sound," *AIAA Journal*, Vol. 32, No. 5, 1994, pp. 897–906.

[7]Bailly, C., Bechara, W., Lafon, P., and Candel, S., "Jet Noise Predictions Using a k–ϵ Turbulence Model," AIAA Paper 93-4412, Oct. 1993.

[8]Bechara, W., Lafon, P., Bailly, C., and Candel, S., "Application of a k–ϵ Turbulence Model to the Prediction of Noise for Simple and Coaxial Free Jets," *Journal of the Acoustical Society of America*, Vol. 97, No. 6, 1995, pp. 3518–3531.

[9]Bailly, C., and Lafon, P., "Computation of Subsonic and Supersonic Jet Mixing Noise Using a Modified k–ϵ Model for Compressible Free Shear Flows," *Acta Acustica*, Vol. 2, 1994, pp. 101–112.

[10]Stoker, R. W., and Smith, M. J., "An Evaluation of Finite Volume Direct Simulation and Perturbation Methods in CAA Applications," AIAA Paper 93-0152, Jan. 1993.

[11]Lighthill, M. J., "On Sound Generated Aerodynamically, I. General Theory," *Proceedings of the Royal Society of London*, Vol. 221A, No. 1107, 1952, pp. 564–587.

[12]Viswanathan, K., Sankar, R., and Reddy, N. N., "A Fluid Acoustic Coupled Simulation of Supersonic Jet Noise," AIAA Paper 94-0137, Jan. 1994.

[13]Shih, S. H., Hixon, D. R., and Mankbadi, R. R., "Zonal Approach for Prediction of Jet Noise," *Journal of Propulsion and Power*, Vol. 13, No. 6, 1997, pp. 745–752.

[14]Lyrintzis, A. S., and Mankbadi, R. R., "On the Prediction of the Far-Field Jet Noise Using Kirchhoff's Formulation," AIAA Paper 95-0508, Jan. 1995.

[15]Soh, W. Y., "Unsteady Jet Flow Computation Towards Noise Prediction," AIAA Paper 94-0138, Jan. 1994.

[16]Gottlieb, D., and Turkel, E., "Dissipative Two-Four Methods for Time Dependent Problems," *Mathematics of Computation*, Vol. 30, No. 136, 1976, pp. 703–723.

[17]Bayliss, A., Parikh, P., Maestrello, L., and Turkel, E., "A Fourth-Order Scheme for the Unsteady Compressible Navier–Stokes Equations," AIAA Paper 85-1694, June 1985.

[18]Ducros, F., "Simulations numériques directes et des grandes échelles de couches limites compressibles," Ph.D. Thesis, Laboratoire d'Études des Ecoulements Géophysiques et Industriels, Inst. de Mécanique de Grenoble, Grenoble, France, Nov. 1995.

[19]Ragab, S. A., and Sheen, S. C., "Large-Eddy Simulation of a Mixing Layer," AIAA Paper 91-0233, Jan. 1991.

[20]Ragab, S. A., Sheen, S. C., and Sreedhar, M., "An Investigation of Finite-Difference Methods for Large-Eddy Simulation of a Mixing Layer," AIAA Paper 92-0554, Jan. 1992.

[21]Tang, W., Komerath, N., and Sankar, L., "Numerical Simulation of the Growth of Instabilities in Supersonic Free Shear Layers," AIAA Paper 89-0376, Jan. 1989.

[22]Sankar, L. N., Reddy, N. N., and Hariharan, N., "A Comparative Study of Numerical Schemes for Aeroacoustic Applications," *Computation Aero- and Hydro-Acoustics*, FED-Vol 147, American Society of Mechanical Engineers, Fairfield, NJ, 1993.

[23]Hayder, M. E., and Turkel, E., "Boundary Conditions for Jet Flow Computations," AIAA Paper 94-2195, June 1994.

[24]Gamet, L., and Estivalezes, J. L., "Non-Reflexive Boundary Conditions Applied to Jet Aeroacoustics," AIAA Paper 95-0159, Jan. 1995.

[25]Gamet, L., "Simulations numériques d'écoulements compressibles. Application à l'aéroacoustique des jets," Ph.D. Thesis, Ecole Nationale de l'Aéronautique et de l'Espace, Toulouse, France, April 1996.

[26]Hixon, D. R., Shih, S. H., and Mankbadi, R. R., "Evaluation of Boundary Conditions for Computational Aeroacoustics," AIAA Paper 95-0160, Jan. 1995.

[27]Scott, J. N., Mankbadi, R. R., Hayder, M. E., and Hariharan, S. I., "Outflow Boundary Conditions for the Computational Analysis of Jet Noise," AIAA Paper 93-4366, Oct. 1993.

[28]Thompson, K. W., "Time Dependent Boundary Conditions for Hyperbolic Systems I," *Journal of Computational Physics*, Vol. 68, 1987, pp. 1–24.

[29]Thompson, K. W., "Time Dependent Boundary Conditions for Hyperbolic Systems II," *Journal of Computational Physics*, Vol. 89, 1987, pp. 439–461.

[30]Giles, M., "Non-Reflecting Boundary Conditions for the Euler Equations," Computational Fluid Dynamics Lab., TR CFDL-TR-88-1, Massachusetts Inst. of Technology, Cambridge, MA, Feb. 1988.

[31]Giles, M., "Non-Reflecting Boundary Conditions for Unsteady Airfoil Calculations," Computational Fluid Dynamics Lab., TR CFDL-TR-90-1, Massachusetts Inst. of Technology, Cambridge, MA, Feb. 1990.

[32]Giles, M., "Non-Reflecting Boundary Conditions for Euler Equation Calculations," *AIAA Journal*, Vol. 28, No. 12, 1990, pp. 2050–2058.

[33]Poinsot, T. J., and Lele, S. K., "Boundary Conditions for Direct Simulations of Compressible Reacting Flows," TR 100010, Stanford Univ. and NASA Ames Research Center, Stanford, CA, 1990.

[34]Rudi, D. H., and Strikwerda, J. C., "A Non-Reflecting Outflow Boundary Condition for Subsonic Navier–Stokes Calculations," *Journal of Computational Physics*, Vol. 36, No. 1, 1980, pp. 55–70.

[35]Vreman, A. W., "Direct and Large-Eddy Simulation of the Compressible Turbulent Mixing Layer," Ph.D. Thesis, Dept. of Applied Mathematics, Univ. of Twente, Twente, The Netherlands, Dec. 1995.

[36]Comte, P., Ducros, F., Silvestrini, J., David, E., Lamballais, E., Metais, O., and Lesieur, M., "Simulations des Grandes Echelles d'Ecoulements Transitionnels," *Proceedings of the 74th AGARD Fluid Dynamics Meeting* (Chania, Greece), CP-551, AGARD, Dec. 1994.

[37]Ducros, F., Comte, P., and Lesieur, M., "Large-Eddy Simulation of a Weakly-Compressible Boundary Layer Spatially Developing over an Adiabatic Flat Plate," *Proceedings of the International Symposium on Turbulence, Heat and Mass Transfer*, Lisbon, Portugal, 1994.

[38]Ducros, F., Comte, P., and Lesieur, M., "Large Eddy Simulations of Transition to Turbulence in a Weakly Compressible Boundary Layer over a Flat Plate," *Journal of Fluid Mechanics*, Vol. 326, 1996, pp. 1–36.

[39]Erlebacher, G., Hussaini, M. Y., Speziale, C. G., and Zang, T. A., "Towards the Large-Eddy Simulation of Compressible Turbulent Flows," *Journal of Fluid Mechanics*, Vol. 238, 1992, pp. 155–185.

[40]Metais, O., and Lesieur, M., "Spectral Large-Eddy Simulation of Isotropic and Stably Stratified Turbulence," *Journal of Fluid Mechanics*, Vol. 239, 1992, pp. 157–194.

[41]Lesieur, M., Metais, O., Normand, X., and Silveira-Neto, A., "Spectral Large Eddy Simulation of Turbulent Shear Flows," *Large Eddy Simulation of Complex Engineering and Geophysical Flows*, edited by Boris Galerpin and Steven A. Orszag, Cambridge Univ. Press, Cambridge, England, UK, 1993, pp. 179–192.

[42]Kraichnan, R. H., "Eddy Viscosity in Two and Three Dimensions," *Journal of Atmospheric Sciences*, Vol. 33, 1976, pp. 1521–1536.

[43]Chollet, J.-P., and Lesieur, M., "Parameterization of Small Scales of Three-Dimensional Isotropic Turbulence Utilizing Spectral Closures," *Journal of Atmospheric Sciences*, Vol. 38, 1981, pp. 2747–2757.

[44]Ducros, F., Comte, P., and Lesieur, M., "Direct and Large-Eddy Simulations of Transition of a Supersonic Boundary Layer," *Proceedings of the 9th Turbulent Shear Flow Symposium*, 1993.

[45]Normand, X., and Lesieur, M., "Direct and Large-Eddy Simulation of Transition in the Compressible Boundary Layer," *Theoretical and Computational Fluid Dynamics*, Vol. 3, 1992, pp. 231–252.

[46]Comte, P., Silvestrini, J., and Lamballais, E., "A Straightforward 3D Multi-Block Unsteady Navier–Stokes Solver for Direct and Large Eddy Simulation of Transitional and Turbulent Compressible Flow," *Proceedings of the 77th AGARD Fluid Dynamics Meeting* (Seville, Spain), CP-578, AGARD, 1995.

[47]Morino, L., "Mathematical Foundations of Integral Methods," *Computational Methods in Potential Aerodynamics*, Springer–Verlag, New York, 1985, pp. 271–291.

[48]Lyrintzis, A. S., "Review: The Use of Kirchhoff's Method in Computational Aeroacoustics," *Journal of Fluids Engineering*, Vol. 116, Dec. 1994, pp. 665–676.

[49]Freund, B. J., Lele, S. K., and Moin, P., "Calculation of the Radiated Sound Field Using an Open Kirchhoff Surface," Confederation of European Aerospace Societies/AIAA Paper 95-061, 1995.

[50]Seiner, J. M., and Ponton, M. K., "The Effects of Temperature on Supersonic Jet Noise Emission," Deutsche Gesellschaft für Luft- und Raumfahrt/AIAA Paper 92-02-046, 1992.

[51]Seiner, J. M., "Fluid Dynamics and Noise Emission Associated with Supersonic Jets," *Studies in Turbulence*, Springer–Verlag, New York, 1992, pp. 297–323.

[52]Phillips, O. M., "On the Generation of Sound by Supersonic Turbulent Shear Layers," *Journal of Fluid Mechanics*, Vol. 9, No. 1, 1960, pp. 1–28.

[53]Ffowcs Williams, J. E., "The Noise from Turbulence Convected at High Speed," *Philosophical Transactions of the Royal Society of London*, Vol. A-1061, No. 255, 1963, pp. 641–657.

[54]Oertel, H., "Coherent Structures Producing Mach Waves Inside and Outside of the Supersonic Jet. Structure of Complex Turbulent Shear Flow," *IUTAM Symposium, Marseille, France*, 1982, pp. 334–343.

[55]Oertel, H., "Measured Velocity Fluctuations Inside the Mixing Layer of a Supersonic Jet," *Recent Contributions to Fluid Mechanics*, Springer–Verlag, Berlin, 1982, pp. 170–179.

[56]Tam, C. K. W., and Hu, F. Q., "On the Three Families of Instability Waves of High-Speed Jets," *Journal of Fluid Mechanics*, Vol. 201, 1989, pp. 447–483.

S. Glegg
Associate Editor